

Measurement of refractive index and equation of state in dense He, H₂, H₂O, Ne under high pressure in a diamond-anvil cell

A. Dewaele,¹ J. Eggert,¹ P. Loubeyre,¹ and R. Le Toullec^{1,2}

¹*DIF/DPTA, CEA 91680 Bruyères-le-Châtel, France*

²*Université Pierre et Marie Curie, Physique des Milieux Condensés, T13, E4, B77, 4 Place Jussieu, 75252 Paris Cedex 05, France*

(Dated: October 10, 2019)

We present an accurate determination of the refractive index of hydrogen, helium, H₂O and neon up to 35 GPa at ambient temperature. The experimental method is based on the combination of two interferometric signals of the Fabry-Perot cavity containing the sample in the diamond anvil cell. The data are put in perspective through the variation of the molecular polarisability with density. Significant electronic changes are observed. Interesting possibilities of the method are also illustrated: the high precision to finely probe phase transition; the simultaneous measurement of the volume to obtain the equation of state of transparent media with around 1% accuracy.

PACS numbers: 07.35.+k, 64.30.+t, 78.20.-e

I. INTRODUCTION

There exist considerable evidences that pressure can dramatically change the electronic properties of a system. On the atomic scale, the variation of the electronic kinetic and potential energies with volume tends to make a contraction of the atomic size and a delocalisation of valence electrons. Consequently, spectacular transformations have been observed, such as rehybridization of atomic orbitals, like in carbon (sp²) to (sp³) across the graphite to diamond transition ; insulator-metal phase transitions, like in O₂¹, Xe² or CsI³; the transformation of ice from an hydrogen bonded solid to an ionic solid in symmetric ice⁴. Although most changes of the properties of a system under pressure are related to the microscopic electronic reorganization, the determination of the refractive index over a large frequency domain is probably the most direct method to probe the electronic structure. The refractive index expresses the response of the distribution of charges to a perturbing electric field. In order to extract a detailed change of the charge distribution of a system with pressure through the measurement of the refractive index, a large frequency domain has to be investigated. This is unfortunately very difficult at high pressure. However, already interesting electronic evolutions have been obtained from measurements of the refractive index performed in the visible such as in hydrogen with the closure of an electronic transition that parallel the evolution of the electronic gap (see references below).

Also, an accurate determination of the refractive index under pressure has a clear metrological importance. In Brillouin spectroscopy, where the refractive index of the sample and of the pressure transmitting medium have to be known to extract the sound velocity from the frequency shift. In the newly developed laser shock measurements on pre-compressed targets to extract the shock front velocity from the phase shift of the VISAR (velocity interferometric system for any reflector) diagnostics⁵.

Finally, to measure easily the thickness of the sample chamber in the diamond-anvil cell (DAC) with a single spectrometer, when the sample or the pressure transmitting medium is transparent. This can be directly used to measure the Equation of State (EoS) of the sample (see below), or help to control the experimental conditions, for instance by evaluating the strain of the studied sample.

In the DAC, the tips of the diamond anvils that enclose the sample form a Fabry-Perot interferometer. This geometry have already been exploited to measure the refractive index of transparent samples at high pressure. Most of the experimental methods developed so far have been based on the measurement of fringes contrast (^{6, 7, 8, 9}). Other were based on a controlled sample thickness (^{10, 11}). In one work¹², the combination of the measurement of parallel white beam interference spectrum and convergent monochromatic beam interference rings allowed the determination of both refractive index *n* and thickness *t* of the sample. We present here an improvement of this method.

With this setup, we have also been able to measure the Equation of State of helium, by estimating the sample chamber volume changes upon compression. Such a method has been previously described for H₂^{7, 9}. We show here that with numerical photograph technology and the accurate determination of the refractive index, its accuracy is comparable to other techniques. Therefore, it becomes an interesting alternative to X-Ray methods (X-Ray diffraction and X-Ray absorption¹³) for lights elements, particularly light liquids, or to adiabatic compressibility measurement of Brillouin spectroscopy¹⁴.

Three goals have mainly motivated the present accurate refractive index measurements on four systems, He, H₂, Ne and H₂O. First, H, He and H₂O are the main constituents of planetary interiors and the determination of their properties up to planetary core conditions is motivating a lot of effort. Second, He and Ne are the most commonly used quasi-hydrostatic pressure transmitting media at high pressure. In both cases, the determination

of the refractive index should be useful to analyze some spectroscopic measurements. Finally, they have simple electronic structures with different electronic organisations and the present data set could be interesting to test the confidence of *ab-initio* calculations in predicting the optical properties.

The experimental method and a discussion of the uncertainties is presented in section II. The refractive index measurements are presented in section III. The analysis of the data in terms of the changes in the polarizability with density is presented in section IV. Applications of the method to the determination of the equation of state and to the study of phase transitions are described in section V.

II. EXPERIMENTAL PROCEDURE

A. High pressure techniques

In these experiments we used a membrane diamond anvil cell described elsewhere⁽¹⁵⁾ with a large optical aperture ($\pm 30^\circ$) and equipped with 400 or 500 μm table diamonds. Samples have been loaded in a rhenium gasket at room temperature, by the use of high pressure loading techniques. In the case of H_2O , ultra-pure water was inserted in the gasket hole using a syringe. As explained below, thick samples are needed for a better accuracy of the refractive index measurements. For this reason, double rhenium gaskets have been used in the highest pressure runs. These gaskets are prepared in the following manner: two rhenium gaskets are pre-indented, then polished on one side and glued together. With this method, the thickness of an helium sample was of the order of 50 μm at 200 kbar, 30 % more than with a simple gasket. The pressure gauge was ruby, calibrated with the quasi-hydrostatic pressure scale¹⁶, that allows pressure measurement with an accuracy of the order of 0.5 kbar. The absolute accuracy is the one of the ruby scale, *i.e* at maximum 2% over the pressure range investigated here.

B. White light interferences

The refractive index setup is modified from LeToullec *et al.*'s one (see Fig. 1). The white light interference pattern in transmission is recorded over the range 500nm to 700nm with a double subtractive spectrometer (Dilor). A small area, varying between 20 x 20 and 10 x 10 μm^2 , was selected to perform the measurement. Under high pressures ($P > 250$ kbar), the contrast drastically decreased out of a central flat region, because of the strain of the diamonds under pressure. The wavelength difference between two intensity maxima :

$$\Delta\lambda = \frac{\lambda^2}{2n(\lambda)t},$$

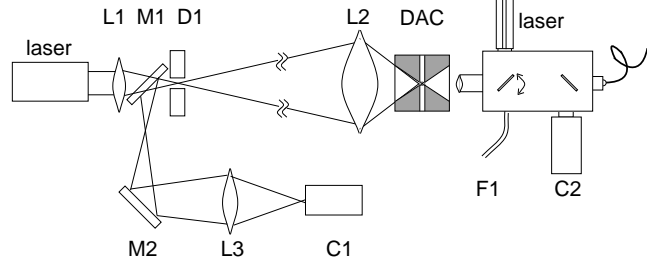


FIG. 1: Experimental setup. The light emitted by the laser 1 (He-Ne, 7 mW or Ar) is extended by L1 (simple lens, $f = 30$ mm) and focused on the sample by the objective L2 ($f = 50$ mm); interference rings propagate through L2, M1, M2, L3 (objective, $f = 80$ mm) and are recorded by the digital camera C1. On the right, the PRL setup (doubled YAG laser, F1: illuminating optical fiber, C2: digital camera, S: spectrometer optical fiber) equipped with a $\times 20$ Mitutoyo objective, allows pressure measurement, imaging of the sample and white light interferences measurement.

where t is the thickness of the sample, $n(\lambda)$ its refractive index, was determined as a function of the wavelength.

C. Monochromatic interferences

The setup presented on Fig. 1 allows the measurement of the reflective Fabry-Pérot rings produced by the cavity between the diamonds, when illuminated by a convergent monochromatic beam. We used an Argon laser ($\lambda = 488.0$ nm) for helium samples 1 to 3, and a He-Ne laser ($\lambda = 632.8$ nm) for H_2O , H_2 , Ne and He-4 samples.

The interference order k at angle i is defined by:

$$k = \frac{1}{\lambda} 2t(n^2 - \sin^2 i)^{1/2}; \quad (1)$$

if k is an integer, a minimum in intensity is observed.

At the center of the pattern, the interference order $k_0 = 2n(\lambda)t/\lambda$, can be deduced from white light interferences measurement. The angular position i_p of the p^{th} intensity minimum has an interference order $k_p = [k_0] - p + 1$. Refractive index and thickness can be deduced from two fringes (p and p') angular positions:

$$n^2 = \frac{k_{p'}^2 \sin^2 i_p - k_p^2 \sin^2 i_{p'}}{k_{p'}^2 - k_p^2} \quad (2)$$

and

$$t^2 = \frac{\lambda^2}{4} \frac{k_{p'}^2 - k_p^2}{\sin^2 i_p - \sin^2 i_{p'}} \quad (3)$$

Interference rings were projected and recorded by a CCD camera (C1, see Fig. 1). The radius R_p of the rings on C1 is thus measured. Because of optical aberrations, mainly caused by the objective lenses L2, the relationship between R_p and i_p was non trivial. To correct these aberrations, a reference spectrum was recorded. This spectrum

consisted in fringes formed by an empty indented and drilled gasket, placed in the DAC. The adjustment of the optical setup was performed as it is described herebelow. First, the cell was centered and perpendicularly oriented on the laser beam. Then M1, C1, L3, L2, L1 and D1 were positioned and the calibration spectrum recorded. All these elements were mounted on linear and rotation stages. After calibration, all the elements, except the cell, remained fixed. In the first experiments, the cell was regularly removed to record the white light interferences pattern. The best position of the cell (in the x direction) was determined, within $\pm 10 \mu\text{m}$, by optimization of the rings pattern stability with respect to Y and X translations. This allowed a reproducibility of the index measurement of $\Delta n = \pm 5.10^{-4}$. Each digital Fabry-Perot pattern was automatically processed by a program that evaluates thickness and index for all available pair of rings. This procedure allows the analysis of numerous spectra, and again, optimization of the x position if the sample. Tentative error bars have been estimated for each measurement, taking into account two factors: first, the uncertainty on rings radius R_p ; second, the scatter of the refractive index given by different couples of rings (Eq. 2).

The precision of refractive index measurements is limited by the following effects:

- precision of k_0 measurement by white light interferences. The relative precision on k_0 estimate is better than 10^{-3} ($\Delta k < 0.2$) for weakly dispersive media (He and H_2) and of approximately 2.10^{-3} for dispersive media (H_2O). This measurement must also be carried out in the same sample region than the region illuminated by the laser beam for monochromatic interferences, in order to prevent any error caused by non-parallelism of the diamonds.

- number of Fabry-Pérot rings: as pointed out by LeToullec *et al.*, the rings must be as numerous as possible to statistically increase the precision of the measurement. In these experiments, a minimum of four rings has been observed. For this purpose, the angular aperture of the optical setup was increased to 25° . The number of rings is also proportional to the sample thickness; therefore, thick samples have been used.

- elastic strain (cupping) of the diamonds. This is the main source of uncertainty of our measurements, that limits the pressure range of this method. This cupping can be first observed by translating the cell in y or z directions and looking at the modification of the rings pattern. It can be noted that these measurements constitute an accurate mean of studying the strain of the anvils. At the beginning of the compression, inverse cupping, caused by the gasket strength, is observed. Upon pressure increase, the diamonds become flat and then cupping occurs. It has been observed approximately at the same thickness of a simple rhenium gasket (40 to 45 μm for H_2O samples), and for pressures varying between 100 and 200 kbar. When pressure increases, it perturbs the rings pattern out of a central flat zone, up to a point

that makes measurements impossible. To reduce this intrinsic limitation, thick gaskets can be used because they increase the pressure at which cupping appears. This elastic strain also makes the focusing diagnostic less precise.

- pressure gradients: the ruby chip could not be directly located where the sample was illuminated, because it perturbs the Fabry-Pérot interferometric rings. It was located at $\simeq 60 \mu\text{m}$ from the refractive index measurement point. In separate runs we have estimated the radial pressure gradient in ice VII, in the same sample geometry; this gradient is negligible up to 200 kbar and reaches $0.33 \text{ kbar}/\mu\text{m}$ at 350 kbar. In ice, the pressure was corrected by this factor. Actually, this pressure gradient is also an intrinsic limitation of the method, because the extend of the source of interference rings is $100 \mu\text{m}$, if $i < 25^\circ$; at high pressure, rings with $i < 15^\circ$ are analyzed in order to reduce this error.

D. EoS measurement

An analysis of numerical images of the sample taken in transmitting light allows the measurement of the surface S of the sample, with a precision of 1 %. The volume V_S is then obtained by multiplying S with the thickness of the sample, obtained at the same time as its refractive index. The uncertainty on volume determination is mainly caused by the uncertainty on S . No corrections taking into account the cupping of the diamond was necessary for the measurements presented in Sec. V, but these corrections are in principle possible. We made the assumption that the amount of matter trapped in the sample chamber remained constant upon pressure increase. In that case, the EoS $V(P)$ can be simply deduced from $V_S(P)$ by choosing a reference point $V_0(P_0)$. For a given run, the molar volume of the sample can be expressed as:

$$V_{\text{mol}}(P) = V(P) \frac{V_{\text{mol}}(P_{\text{ref}})}{V(P_{\text{ref}})},$$

$V(P)$ being the volume of the sample at the pressure P and $V(P_{\text{ref}})$ the volume of the sample at the reference pressure P_{ref} . We noticed that the precision of the volume measurement increased when the thickness of the sample decreases. A similar observation has already been made by Evans and Silvera, 1998,⁹. This is probably because the geometrical imperfections of the gasket hole already extensively described⁷ are smaller for thin samples.

III. REFRACTIVE INDEX DATA

A. Helium

The refractive index data obtained in 4 runs up to 210 kbar are shown in Fig. 2. During the same experimental

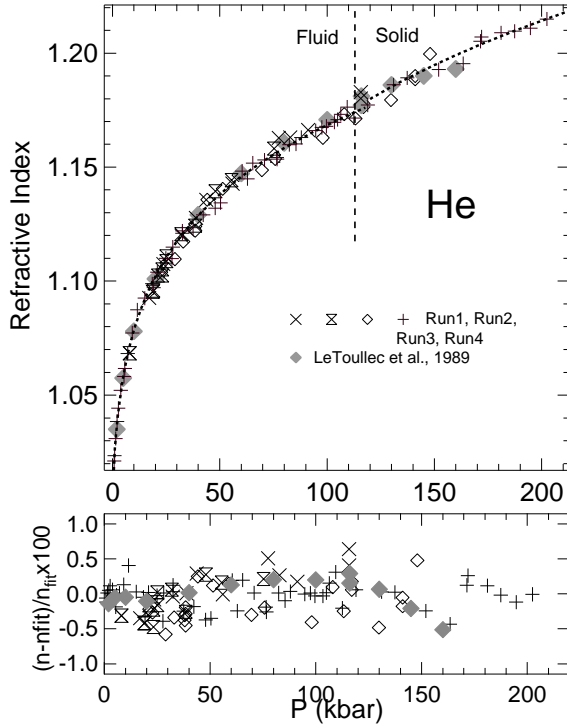


FIG. 2: **Upper:** Refractive index of fluid and solid He as a function of pressure at ambient temperature. The first 3 runs have been performed at $\lambda = 488$ nm, and the last one at $\lambda = 632.8$ nm. The parameters of the fitted functions (dotted lines) are presented in Table I. **Lower:** Difference, in %, between experimental data and the fitted function.

run, the orders of interference of the rings of the fringe pattern have been followed between each pressure steps. The good agreement between the data of the different runs data indicates that the uncertainty associated to the white light determination of the order of interference is negligible. For all data shown in Fig. 2, the error bars are smaller than the size of the symbols. The difference between the fitted index law and LeToullec measurements is smaller than 2.10^{-3} , except for the highest pressure points where LeToullec measurements were less precise.

B. Neon

One run has been performed with a neon sample, up to 27 GPa. The evolution of the refractive index of neon with pressure is plotted in Fig. 3. The refractive index of Ne had been determined previously to a maximum pressure of 1 GPa from capacitance measurements ¹⁷. The present data are in very good agreement with this previous determination, in the pressure range of overlap.

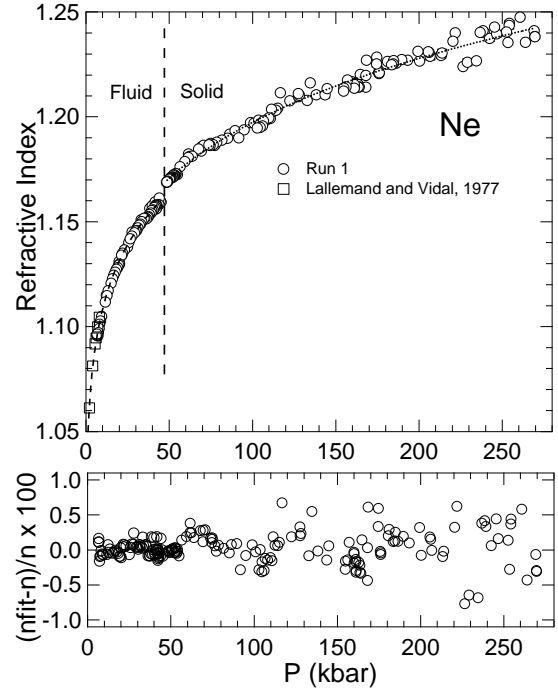


FIG. 3: Same as Fig. 2. Experiments have been performed at $\lambda = 633$ nm. The evolution of sample thickness upon pressure increase and decrease is also represented.

C. Hydrogen

The evolution of the refractive index of hydrogen with pressure is plotted in Fig. 4.

There is a systematic difference between our data and previous determinations, either the one by brillouin scattering ¹⁸ (1.5 %) or the one by white light interference ⁹ (around 1 %, which is within their estimated error bars). The matching of refractive index of ruby and hydrogen has been observed (annulation of the contrast) at 35 ± 10 GPa. This provides an anchorage point to the refractive index curve. At this pressure, the refractive index of ruby is expected to be 1.77 ¹¹; this value is in good agreement with the present measurements and that gives a good confidence in our highest pressure runs.

D. Water and ice

For H_2O , 5 experimental runs have been made, up to 35 GPa. Due to the dispersion of the refractive index of H_2O , of the order of 1 % over the 500 - 800 nm range, the determination of the order of interference from white light measurements is less precise and consequently small deviations between different experimental runs can be detected in the fluid phase. However, our measure-

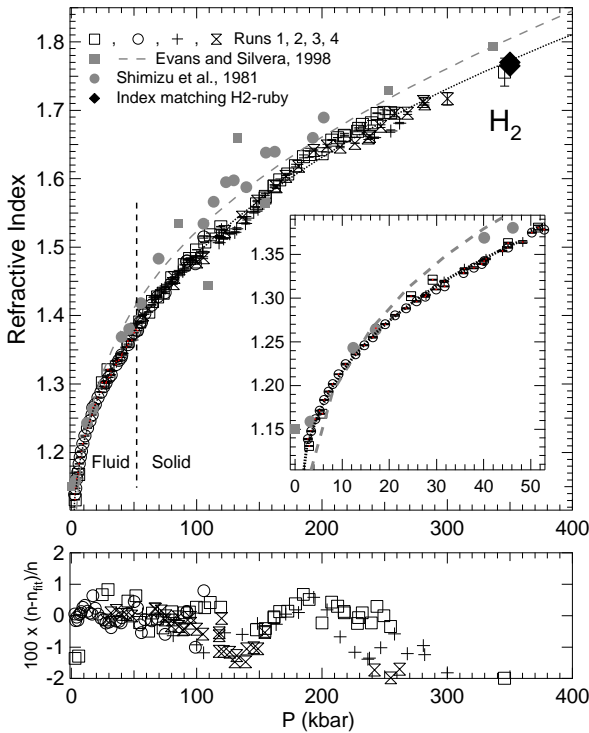


FIG. 4: Refractive index of H_2 at $\lambda = 632.8$ nm. **Inset:** enlarged region in the fluid phase.

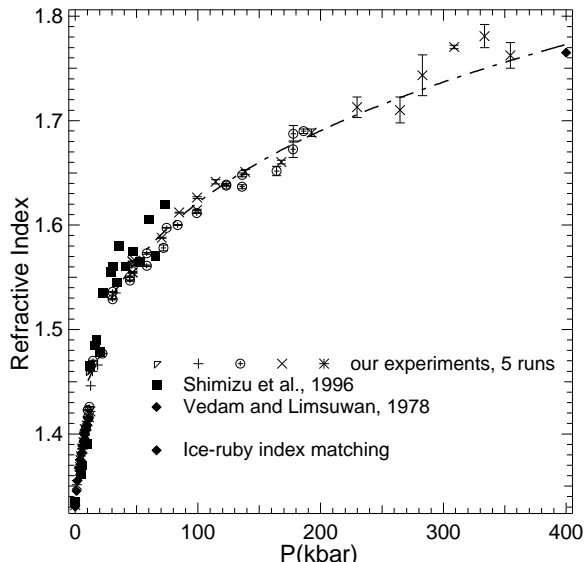


FIG. 5: Measured refractive index of water, ice VI and ice VII, at $\lambda = 632.8$ nm, with the corresponding fitted functions (dotted lines).

Compound	Refractive index	P range (kbar)
Fluid He	$n = 0.8034 + 0.20256(1 + P)^{0.12763}$	0.8-115
Solid He	$n = -0.1033 + (1 + P)^{0.052}$	117-202
Fluid Ne	$n = 0.67 + 0.33(1 + 4.3 \times P)^{0.076}$	7-47
Solid Ne	$n = 0.9860 + 0.08578 P^{0.1953}$	50-270
Fluid H_2	$n = 0.949 + 0.06829(1 + 11.8 P)^{0.2853}$	3-49
Solid H_2	$n = 0.95 + 0.1144 P^{0.3368}$	52-350
Fluid H_2O	$n = 0.900 + 0.4323(1 + 0.1769 P)^{0.164}$	0.5-12
Ice VI	$n = 1.425 + 0.00255 P$	12.7-22
Ice VII	$n = 1.175 + 0.2615(1 + 0.101 P)^{0.222}$	30-354

TABLE I: Fitted forms of refractive index vs. P (in kbar).

ments agree very well with precise interferometric measurements in the fluid phase¹⁹. At higher pressures, our data are within the scatter of a previous Brillouin scattering determination²⁰. At pressures higher than 20 GPa, the strength of ice causes pressure gradients in the sample, that can perturb the pressure estimation. To correct it, the pressure measured by the ruby chip P_R was then corrected by a factor $\Delta P = d \times dP/dr$, d being the distance between the ruby chip and the center of the sample, and the last factor has been estimated in a separate run by mapping the sample chamber with ruby (in kbar/ μm): $dP/dr = (P_R \times 0.425)/t$. The estimated error bars plotted in Fig. 5 increase drastically as pressure increases, showing the decrease of the quality of the fringes pattern associated to the strain of the diamonds. Refractive index matching between ice VII and ruby has been observed at $P = 40.5 \pm 10$ GPa. At this pressure, the refractive index of ruby is approximately 1.765¹¹, 1.2 % lower than the extrapolation of our measurements. That is within the uncertainty of our highest pressure measurements.

The functions obtained by a fitting procedure to our experimental data are gathered in table I. The use of power laws is justified, to a certain extent, by the fact that the Lorentz-Lorenz factor defined in Eq. 4 is approximately constant (see below). We used as least parameters as possible to fit the data. The quality of the various fits is shown in the various figures that present the refractive index of He, H_2 , Ne, H_2O versus pressure.

IV. DISCUSSION

A. Polarizability

The refractive index is generally related to the polarizability of the molecular entities of the system through the Lorentz-Lorenz formulation:

$$LL = \frac{1 \epsilon - 1}{\rho \epsilon + 2} = \frac{4\pi N_A}{3} \alpha. \quad (4)$$

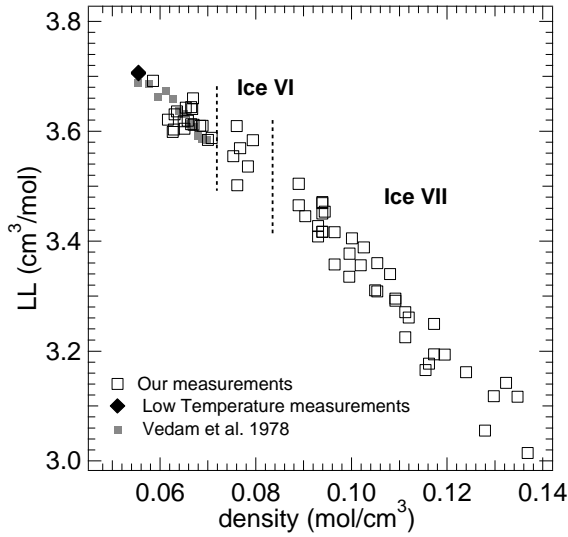


FIG. 6: Lorentz-Lorenz factor of H_2O phases as a function of molar density.

In Eq. 4, N_A is the Avogadro number, ϵ the relative dielectric constant, and α the molecular polarizability of the compound. In the static case, this equation is called the Clausius-Mossotti relation. It arises from the expression of the local electrical field for dense materials: $\mathbf{E}_{\text{loc}}(\mathbf{r}) = \mathbf{E}_{\text{macro}}(\mathbf{r}) + 4\pi\mathbf{P}(\mathbf{r})/3 + \mathbf{E}'(\mathbf{r})$. $\mathbf{P}(\mathbf{r})$ is the polarization and $\mathbf{E}'(\mathbf{r})$ is the field created by the close neighbors of the electronic cloud centered on \mathbf{r} . Eq. 4, corresponds to $\mathbf{E}'(\mathbf{r}) = 0$. This is the case on symmetry center of a cubic crystal. For hydrogen, helium and neon, Eq. 4 is commonly used^{9, 12} because they are constituted by spherical molecular entities (in the case of hydrogen the molecules are freely rotating), organized in highly symmetric structures. Also, for these systems in the pressure range covered here, the electronic transitions are far from the visible. The imaginary part of the refractive index should then be very small and $\epsilon = n^2$ is a very good approximation.

In the case of water, the polarizability is generally written as the sum of three components: the polarizability due to the orientation of the permanent dipole of the water molecule, the polarizability due to the electronic changes associated to the inter and intra-molecular modes and the polarizability associated to the electronic transitions within the water molecules. The contribution of the permanent dipoles operates at frequencies below 10^5 Hz. The contribution due to the intermolecular modes is important below 10^{11} Hz in the liquid and 10^5 Hz in the solid²¹. The contributions due to the intra-molecular modes should be important below 10^{14} Hz (the highest frequency vibration mode of H_2O is a stretching mode at 3656 cm^{-1} in the gas phase). Above 10^{16} Hz electronic transitions should be considered. The optical window covered here is just in between these dis-

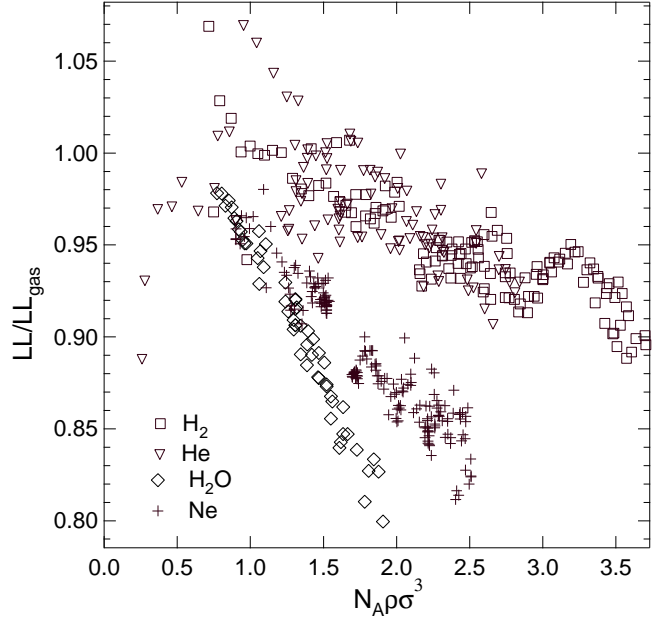


FIG. 7: Lorentz-Lorenz functions of the studied compounds, normalized to their gas value^{26, 17, 27}.

persion phenomena, which implies a small dispersion of the refractive index and a small absorption. We did not observe any pressure effect on the dispersion. In Fig. 6, the Lorentz-Lorenz factor of water and ice calculated using the present data and published equations of state of liquid water, Ice VI and Ice VII^(22, 23, 24, 25) is plotted, as a function of molar density ρ . It is interesting to note that the variation of LL plotted on Fig. 6 does not depend on the microscopic arrangement of the molecules but only of the density. This tends to prove that the hypothesis $\mathbf{E}'(\mathbf{r}) = 0$ in the local field is also reasonably valid in water. Consequently, Eq. 4 should be valid here to analyze the data. It is seen in figure 6 that the LL factor decreases by approximately 20 % up to the maximum pressure of investigation. The approximation LL constant, that is used to analyse spectroscopic data of water under pressure, such as the Brillouin scattering sound velocity measurements¹⁴, is not correct because it leads to an underestimation of the refractive index of the order of 3 % at 35 GPa. It has been proposed from experimental data below 1 GPa, that the evolution of the Lorentz-Lorenz factor of various molecular systems should follow an universal curve when plotted in reduced units¹⁷, and after small statistical dipole-induced dipole corrections. In our case, their relative effect on LL is smaller than 10^{-3} and can be neglected. In figure 7, the change of the Lorentz-Lorenz factors of He, Ne, H_2 , H_2O with density in reduced units, i.e. as LL/LL_{gas} , because LL_{gas} (taken in^{26, 17, 27}) contains the isolated atom polarizability, vs. $N_A \rho \sigma^3$, where σ is the Lennard-Jones parameter of the considered compound. The following Lennard-Jones parameters have been used: He, $\sigma = 2.556\text{ \AA}^{28}$;

Ne , $\sigma = 2.83 \text{ \AA}$, fitted value from²⁹; H_2 , $\sigma = 3.06 \text{ \AA}$, fitted value from³⁰; H_2O , $\sigma = 2.85 \text{ \AA}$ ³¹. Calculations have been performed using the following published EoS:^{12,32} for He ,^{29,17,33,34} for Ne ,^{35,36,37} for H_2 . The scatter of the points give an idea of the experimental errors. The large scatter at low pressure observed for He and H_2 , the most compressible materials, is mainly caused by the uncertainty on density calculation; moreover, uncertainty on LL is larger when n is close to one. At higher compression, relative uncertainty decreases.

On Fig. 7, a common trend is observed, namely a decrease of the polarizability with density in the four systems. In fact, the polarizability is related to the extent of the electronic cloud. In a dense environment, the atoms and molecules themselves compress to lower their interactions with their neighbors, and a decrease of the polarizability is expected. Over the compression range covered here, the scaled LL factors H_2 and He , two isoelectronic species, exhibit the same density evolution. However, in that pressure range, the fundamental difference between the density effect on electronic properties of these two media would be extracted from dispersion data. In He , it has been shown that the main contribution of the change of polarizability with density is taken into account by the blue shift of the $1\text{S}-2\text{P}$ transition energy¹². In contrast, the change of polarizability in hydrogen has been related to the red shift of the excitonic level $X^1\Sigma_g^+$ to $B^1\Sigma_u^+$ that should lead to the metal hydrogen^{38,39}. But different evolutions are observed in Ne and H_2O ; the proposed universal behavior¹⁷ is nor valid nor theoretically justified for a large perturbation by density. In the past 20 years, numerous computations and measurements have been performed for rare gas fluids (see^{40,26,41} and references therein), in order to reproduce, with success for rare-gas fluids, the two and three order refractivity virial coefficients. Yet, they have not been extended in the dense fluid or the solid phases. We are not aware of any calculation on the dielectric properties of water under pressure. On the other hand, the calculation of the dielectric properties of hydrogen is a subject of great current interest (). We present here an interesting database of optical properties of low Z compounds under pressure. We hope that it could be helpful to validate *ab-initio* approaches.

B. Gladstone-Dale relation

The Gladstone-Dale relation expresses as⁴²:

$$\frac{dn}{n-1} = \frac{d\rho}{\rho}, \quad (5)$$

which leads to $n = 1 + a\rho$. It can be derived by differentiating Eq. 4 and expanding it as a function of $u = n - 1$, if the polarizability is assumed to remain constant :

$$\frac{du}{u} \left(1 - \frac{1}{6}u - \frac{5}{6}u^2 + \dots \right) = \frac{d\rho}{\rho}.$$

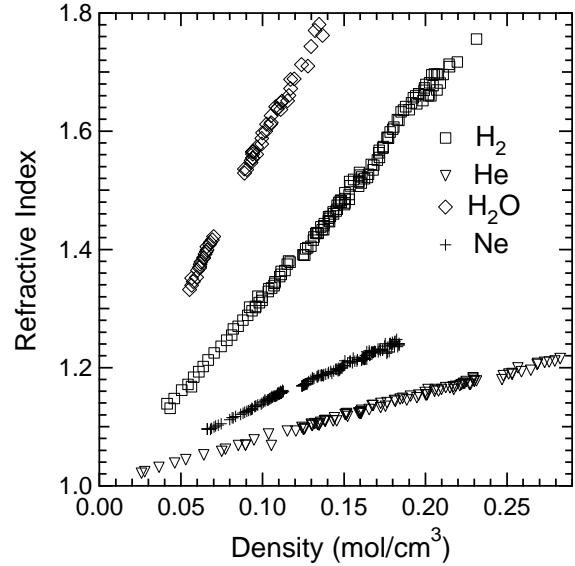


FIG. 8: Refractive index vs. density of the studied compounds. The corresponded fitted linear functions are on table II

Compound	a	$b (\text{cm}^3/\text{mol})$
He	1.005 ± 0.001	0.749 ± 0.006
Fluid Ne	1.000 ± 0.001	1.413 ± 0.009
Solid Ne	1.011 ± 0.003	1.25 ± 0.02
Fluid H_2	0.994 ± 0.003	3.26 ± 0.03
Solid H_2	0.953 ± 0.007	3.53 ± 0.04
Fluid H_2O	1.00 ± 0.01	6.05 ± 0.2
Ice VII	1.081 ± 0.01	5.083 ± 0.13

TABLE II: Density linear evolution of the refractive index obtained in this work ; the index expresses as: $n = a + b\rho$.

Thus, this relation corresponds to the zero-order truncated series expansion of du vs. $d\rho$. For $n < 1.8$, the first order term remains smaller than 13 % of the zero-order term. Moreover, the volume dependency of α will tend to compensate the effect of the first and second order terms.

The Gladstone-Dale relation has been widely used to analyze the shock-wave VISAR data. In fact, a transparent window is often attached to the rear face of the sample, together with an optically reflecting interface, to prevent the formation of a reflected rarefaction wave. The high pressure refractive index of this window is needed to determine the rear face velocity of the sample by VISAR technique⁴². It can also be useful if the sample itself is transparent, and if the shock front becomes reflective. This is the case for pre-compressed samples⁵. An advantage of the Gladstone-Dale relation is that refractive index expresses as a function of the density of the material alone (intrinsic temperature effect is not taken into account), and very simply. In this peculiar

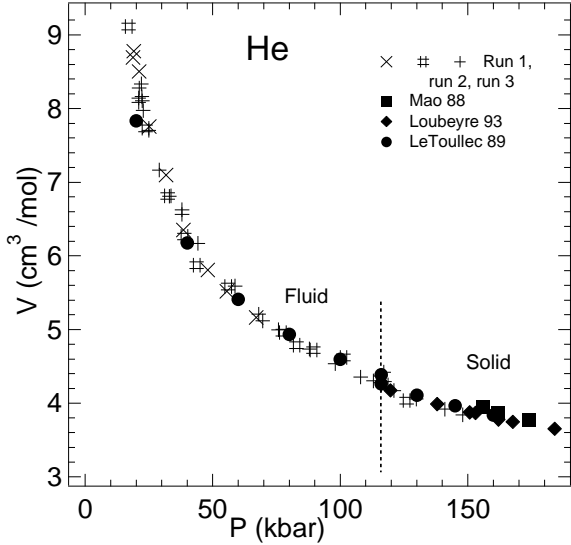


FIG. 9: EoS of helium deduced from the sample thickness evolution upon pressure increase for runs 1, 2 and 3. It compares very well with previous determinations (43, 12, 32), within 1 %, except for the lowest pressures.

form, it allows to express very simply the actual velocity of the reflecting interface as a function of its apparent velocity, for a planar single shock wave.

For this reason, we think that a presentation of our results in a form of Gladstone-Dale fit could be useful for the high pressure community. They are presented in Fig. 8. The data are close to straight lines, even if a small curvature is obvious in all curves. The Gladstone-Dale relation is often used under modified forms, for instance: $n = a + b\rho^{42}$; we fitted our data with this function. The results are presented on Table II.

V. APPLICATIONS

A. Equation of State

The EoS of helium in the fluid and solid phase has been measured up to 13 GPa; they are presented in Fig. 9. Sample thickness was varying between 37 μm and 23 μm (simple gaskets). The evolution of the sample thickness during run 4 (double rhenium gasket) is plotted on Fig. 10. It is interesting to note that the thickness of the sample decreased non-linearly upon pressure increase but remained approximately constant upon pressure decrease: from 47 μm to 48.5 μm . This can be used experimentally, when the sample thickness knowledge is needed¹³: one can perform measurements upon pressure decrease.

At moderate pressures ($P < 3$ GPa), it seems that the compressibility of the sample is overestimated; this effect can be attributed to either leakage of the sample or geo-

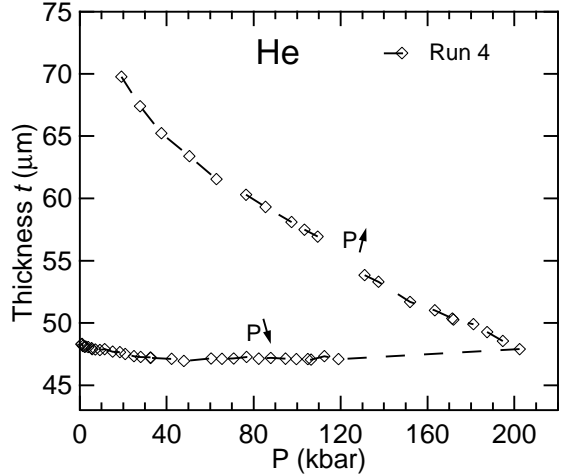


FIG. 10: Evolution of the sample thickness upon pressure increase and decrease for Run 4.

metrical effects. Between 3 and 14 GPa, agreement with LeToullec *et al.*, 1989 calculations is excellent. No evident leakage has been observed in that pressure range. This shows that this method for EoS measurements is valuable for liquids, where X-Ray diffraction measurements are still difficult to perform and where there is no radial pressure gradient in the sample. In particular, these measurements could be carried out for high temperature and high pressure liquids.

B. Detection of phase changes

The volume discontinuities at each phase changes can be deduced from our measurements. In fact, we observed no evidence the the LL factor was discontinuous at any phase change studied. It can thus be assumed to remain constant, and by differentiating Eq. 4, $\Delta\rho/\rho$ can be deduced from the observed Δn . The results are summarized table III. Our data compare very well with those obtained by other techniques. Thus, careful refractive index measurement can detect phase changes with volume changes as small as 2 %.

Phase change P (kbar)	Δn $\times 10^3$	$\Delta\rho/\rho$ (%)	$\Delta\rho/\rho$ literature (%)
Fusion He	116	3 ± 2	2 ± 1.3
Fusion Ne	47.7	6 ± 2	3.5 ± 1.2
Fusion H ₂	53	8 ± 2	3 ± 0.8
Fusion H ₂ O	9.7	41 ± 4	9.7 ± 1
Ice VI \rightarrow VII	21.5	37 ± 4	8.0 ± 0.8

TABLE III: Density discontinuities at phase changes; the temperature of measurements was between 297 and 299 K.

VI. CONCLUSION

We have performed accurate optical refractive index measurements of H₂O, He, H₂ and Ne up to 35 GPa and at ambient temperature in a diamond anvil cell. These data are needed to analyse some spectroscopic measurements on these systems at high pressure. The change of the refractive index has been expressed in terms of the change of the polarizability of the molecular entities in

their dense surroundings. It is still challenging to compute such electronic properties. The present set of data could be useful in validating the various theoretical approaches. Our method also allows the direct measurements of the Equations of State of transparent media: this has been carried out for fluid and solid He, with less than 1 % error. This method could then be interesting to determine the equation of state of dense fluids or dense amorphous media.

¹ S. Desgreniers, Y. Vohra, and A. Ruoff, *J. Phys. Chem.* **94**, 1117 (1990).

² K. A. Goettel, J. H. Eggert, I. F. Silvera, and W. C. Moss, *Phys. Rev. Lett.* pp. 665–668 (1989).

³ M. Eremets, K. Shimizu, T. Kobayashi, and K. Amaya, *Science* **281**, 1333 (1998).

⁴ A. Goncharov, V. Struzhkin, M. Somayazulu, R. Hemley, and H.-K. Mao, *Science* **273**, 218 (1996).

⁵ K. K. M. Lee, L. R. Benedetti, A. Mackinnon, D. Hicks, S. J. Moon, P. Loubeyre, F. Occelli, A. Dewaele, G. W. Lee, and R. Jeanloz, *AIP Conference Proceedings* **620**, 1363 (2002).

⁶ J. VanStraaten, R. Wijngaarden, and I. Silvera, *Phys. Rev. Lett.* **48**, 97 (1982).

⁷ J. V. Straaten and I. F. Silvera, *Phys. Rev. B* **37**, 1989 (1988).

⁸ R. Hemley, M. Hanfland, and H. Mao, *Nature* **350**, 488 (1990).

⁹ W. Evans and I. Silvera, *Phys. Rev. B* **57**, 14105 (1998).

¹⁰ J. Eggert, L. Xu, R. Che, L. Chen, and J. Wang, *J. Appl. Phys* **72**, 2453 (1992).

¹¹ N. Balzaretti, J. Denis, and J. DaJornada, *J. Appl. Phys.* **73**, 1426 (1993).

¹² R. LeToullec, P. Loubeyre, and J. Pinceaux, *Phys. Rev. B* **40**, 2368 (1989).

¹³ G. Shen, N. Sata, M. Newville, M. Rivers, and S. Sutton, *Appl. Phys. Lett.* **81**, 1411 (2002).

¹⁴ M. Grimsditch, S. Popova, and A. Polian, *J. Chem. Phys.* **105**, 8801 (1996).

¹⁵ R. LeToullec, J.-P. Pinceaux, and P. Loubeyre, *High Press. Res.* **1**, 77 (1988).

¹⁶ H.-K. Mao, J. Xu, and P. Bell, *J. Geophys. Res.* **91**(B5), 4673 (1986).

¹⁷ M. Lallemand and D. Vidal, *J. Phys. Chem.* **68**, 4776 (1977).

¹⁸ H. Shimizu, E. Brody, H. Mao, and P. Bell, *Phys. Rev. Lett.* **47**, 128 (1981).

¹⁹ K. Vedam and P. Limsuwan, *J. Chem. Phys.* **69**, 4762 (1978).

²⁰ H. Shimizu, T. Nabetani, T. Nishiba, and S. Sasaki, *Phys. Rev. B* **53**, 6107 (1996).

²¹ F. Petrenko and R. Whitworth, *Physics of Ice* (Oxford University Press, Oxford, 1999).

²² A. Saul and W. Wagner, *J. Phys. Chem. Ref. Data* **18**, 1537 (1989).

²³ P. Bridgman, *Proc. AM. Acad. Arts Sci.* **74**, 399 (1942).

²⁴ R. Hemley, A. Jephcoat, H. Mao, C. Zha, L. Finger, and D. Cox, *Nature* **330**, 737 (1987).

²⁵ P. Loubeyre, R. LeToullec, E. Wolanin, M. Hanfland, and D. Hausermann, *Nature* **397**, 503 (1999).

²⁶ H. Achtermann, J. Hong, G. Magnus, R. Aziz, and M. Slaman, *J. Chem. Phys.* **98**, 2308 (1993).

²⁷ P. Schiebener, J. Straub, J. L. Sengers, and J. Gallagher, *J. Phys. Chem. Ref. Data* **19**, 677 (1990).

²⁸ J. Barker, *Interatomic Potentials for Inert Gases from Experimental Data* (Academic Press, 1976), chap. 4, pp. 212–264.

²⁹ W. Vos, J. Shouten, D. Young, and M. Ross, *J. Chem. Phys.* **94**, 3835 (1991).

³⁰ M. Ross, F. Ree, and D. Young, *J. Chem. Phys.* **79**, 1487 (1983).

³¹ A. Belonoshko and S. Saxena, *Geochim. Cosmochim. Acta* **55**, 381 (1991).

³² P. Loubeyre, R. LeToullec, J.-P. Pinceaux, H.-K. Mao, J. Hu, and R. Hemley, *Phys. Rev. Lett.* **71**(14), 2272 (1993).

³³ L. Finger, R. Hazen, G. Zou, H. Mao, and P. Bell, *Appl. Phys. Lett.* pp. 892–894 (1981).

³⁴ P. Kortbeek, S. Biswas, and J. Schouten, *Int. J. Thermophys.* **803**, 803 (1988).

³⁵ R. Mills, D. Liebenberg, J. Bronson, and L. Schmidt, *J. Chem. Phys.* **66**, 3076 (1977).

³⁶ R. Hemley, H. Mao, L. Finger, A. Jephcoat, R. Hazen, and C. Zha, *Phys. Rev. B* **42**, 6458 (1990).

³⁷ G. Pratesi, L. Ulivi, F. Barocchi, P. Loubeyre, and R. LeToullec, *J. Phys.: Condens. Matter* **9**, 10059 (1997).

³⁸ J. V. Straaten and I. Silvera, *Phys. Rev. B* **37**, 6478 (1988).

³⁹ A. Garcia, M. Cohen, J. Eggert, F. Moshary, W. Evans, K. Goettel, and I. Silvera, *Phys. Rev. B* **45**, 9709 (1992).

⁴⁰ P. Dacre, *Can. J. Phys.* **60**, 963 (1981).

⁴¹ C. Hattig, H. Larsen, J. Olsen, P. Jorgensen, H. Koch, B. Fernandez, and A. Rizzo, *J. Chem. Phys.* **111**, 10099 (1999).

⁴² R. Setchell, *J. Appl. Phys.* **91**, 2833 (2002).

⁴³ H.-K. Mao, R. Hemley, Y. Wu, A. Jephcoat, L. Finger, C. Zha, and W. Basset, *Phys. Rev. Lett.* **60**(25), 2649 (1988).